



## Article

# Exploring the Potential of UAV-Based Hyperspectral Imagery on Pine Wilt Disease Detection: Influence of Spatio-Temporal Scales

Jie Pan <sup>1,2,\*</sup> , Jiayi Lin <sup>1</sup> and Tianyi Xie <sup>1</sup><sup>1</sup> College of Forestry, Nanjing Forestry University, Nanjing 210037, China<sup>2</sup> Co-Innovation Center for Sustainable Forestry in Southern China, Nanjing Forestry University, Nanjing 210037, China

\* Correspondence: panjienfu@njfu.edu.cn; Tel.: +86-139-5198-9205

**Abstract:** Pine wilt disease (PWD), caused by pine wood nematode (PWN, *Bursaphelenchus xylophilus*), poses a serious threat to the coniferous forests in China. This study used unmanned aerial vehicle (UAV)-based hyperspectral imaging conducted at different altitudes to investigate the impact of spatio-temporal scales on PWD detection in an monoculture Masson pine plantation. The influence of spatio-temporal scales on hyperspectral responses of pine trees infected with PWD and detection accuracies were evaluated by Jeffries–Matusita (J-M) distances and the random forest (RF) algorithm. The optimal vegetation indices (VIs) and spatial resolutions were identified by comparing feature importance and model accuracy. The main results showed that the VIs and J-M distances were greatly affected by spatio-temporal scales. In the early, mid-, and late infection stages, the RF-based PWD detection model had accuracies ranging between 72.05 and 79.48%, 83.71 and 89.59%, and 96.81 and 99.28%, peaking at the 10 cm, 8 cm, and 4 cm spatial resolutions, respectively. The green normalized difference vegetation index (GNDVI) and red edge position (REP) were the optimal VIs in early and mid-infection stages, respectively. This study can be important to improve the efficiency of PWD detection and reducing the loss of forests resources.



**Citation:** Pan, J.; Lin, J.; Xie, T. Exploring the Potential of UAV-Based Hyperspectral Imagery on Pine Wilt Disease Detection: Influence of Spatio-Temporal Scales. *Remote Sens.* **2023**, *15*, 2281. <https://doi.org/10.3390/rs15092281>

Academic Editors: Hiep Luong and Klaas Pauly

Received: 24 February 2023

Revised: 6 April 2023

Accepted: 20 April 2023

Published: 26 April 2023



**Copyright:** © 2023 by the authors. Licensee MDPI, Basel, Switzerland. This article is an open access article distributed under the terms and conditions of the Creative Commons Attribution (CC BY) license (<https://creativecommons.org/licenses/by/4.0/>).

**Keywords:** pine wilt disease; UAV-based; hyperspectral; spatio-temporal scale

## 1. Introduction

Pine wilt disease (PWD), caused by the pine wood nematode (PWN), is a highly destructive disease that threatens the forests of East Asia [1–3]. In China, since its first discovery at the Sun Yat-sen Mausoleum of Nanjing in 1982, PWD has rapidly spread and caused irreparable losses [4,5]. The pathogenic pine wood nematode causes pine wilt rapidly and its pathogenesis is complex, which has not been fully understood [6].

Traditional field survey methods to detect PWD are time-consuming and labor-intensive [7]. Therefore, a faster and more effective PWD detection method is needed. Remote sensing are non-contact detection technologies that use spectral information from sensors to indirectly obtain characteristic of target objects [8]. Remote sensing has been widely used in many fields, including flood monitoring [9], land use and land cover survey [10], and plant disease identification [11–13].

After being infected with PWD, changes in physiological variables and leaf cell structure are reflected in the spectral characteristics, which can be used to infer PWD infection status [8,14]. On this basis, there have been numerous studies using multispectral remote sensing to identify trees with late stage PWD infections [15–17]. However, in the early infection stage, multispectral remote sensing cannot distinguish the subtle differences in spectral responses between infected and non-infected trees. Compared with multispectral remote sensing, hyperspectral remote sensing has a much higher spectral resolution, which gives it a significant advantage in distinguishing among subtle spectral changes. Kim et al.

used hyperspectral data to determine the optimal vegetation indices (VIs) for detecting PWD in the early infection stage [7]. The Green-Red Spectral Area Index (GRSAI) they established was able to identify PWD much earlier than other VIs. Zhang et al. established a genetic algorithm-partial least squares regression (GA-PLSR) model based on the hyperspectral data to predict PWD [16]. Yu et al. integrated unmanned aerial vehicle (UAV) based hyperspectral images and ground-based data to determine the accuracy of PWD detection models established by VIs, red edge parameters, moisture indices, and their combinations [18]. Their results showed that the model combining all parameters had the highest accuracy.

Continuous monitoring of trees infected with PWD using remote sensing, especially in the early infection stage, can capture dynamic changes in spectral information and help detect PWD before it spreads to other pine trees. Traditional satellite remote sensing is not suitable for the early detection of PWD due to its fixed return visit period and lack of flexibility [18]. In the past decade, UAV-based remote sensing technology has been widely used in forest disease detection due to its high flexibility, efficiency, and spatial resolution [19–21]. Zhou et al. used UAV-based RGB images to segment and detect individual trees infected by PWD. By using adaptive local threshold selection methods, infected trees in grayscale images could be automatically segmented according to the vegetation index (VEG) with an accuracy of 90% [22]. Deng et al. set up a deep learning framework using faster region convolutional neural networks to detect PWD and the model accuracy reached 90% [23]. The emergence of UAV enables continuous monitoring which facilitates the early detection of PWD, and also enables researchers to obtain images with different spatial resolutions.

Although many studies have used UAV-based data to detect forest diseases, few have focused on the impact of spatio-temporal scales on forest disease monitoring, especially in PWD detection. Guo et al. used UAV-based hyperspectral images to detect wheat yellow rust disease at the field scale [24]. They resampled 1.2 cm spatial resolution images at 3 cm, 5 cm, 7 cm, 10 cm, 15 cm, and 20 cm, and determined that the 10 cm spatial resolution was optimal for detecting wheat yellow rust disease. Jonathan et al. used UAV images, including original images and resampled images, to monitor disease outbreak in mature *Pinus radiata* D. simulated using herbicides [25]. They found that 1 m was the optimal spatial resolution for detecting simulated forest disease in both small and large tree clusters. Zeng et al. used the RGB images of unusual dead pines (dead not due to PWD) collected by UAV at 430 m and 700 m altitudes to monitor PWD [26]. Their results showed that images collected at 430 m and 700 m could both be used to accurately identify unusual dead trees. However, the above studies have only used natural color or multi-spectral images for forest disease detection. In addition, they used resampling to obtain images with different spatial resolutions instead of collecting images at different flight altitudes. However, resampling just simulates the real value through the algorithm, which is still different from the real value and may produce erroneous results.

In this study, UAV-based hyperspectral images collected at different spatio-temporal scales (different spatial resolutions and infection stages) were used to assess the development of PWD. The objectives are: (1) To analyze the impact of spatio-temporal scales on PWD detection; (2) determine the optimal spectral bands, vegetation indices (VIs), and spatial resolution for PWD detection in early, mid-, and late infection stages.

## 2. Materials and Methods

### 2.1. Study Area

The study area covered approximately 1.7 ha of the Baima forestry experimental station in Lishui, Nanjing city, Jiangsu province, China (31°36'47"N, 119°9'32"E) (Figure 1). In this area, the average annual temperature and precipitation were 16 °C and 1147 mm, respectively. The natural period of PWD infection in this area usually spans from the end of June to the beginning of October each year. There were no PWD-infected pine trees in the area before we injected the PWN. During this period, the climate is hot and humid, which is suitable for the reproduction of PWN. However, in the early summer, a continuous rainy

weather period called the “plum rain” occurred in the middle and lower reaches of the Yangtze River in China, which affected data collection in this experiment. To reduce the influence of weather, the experiment was conducted on sunny and cloudless days, as much as possible.

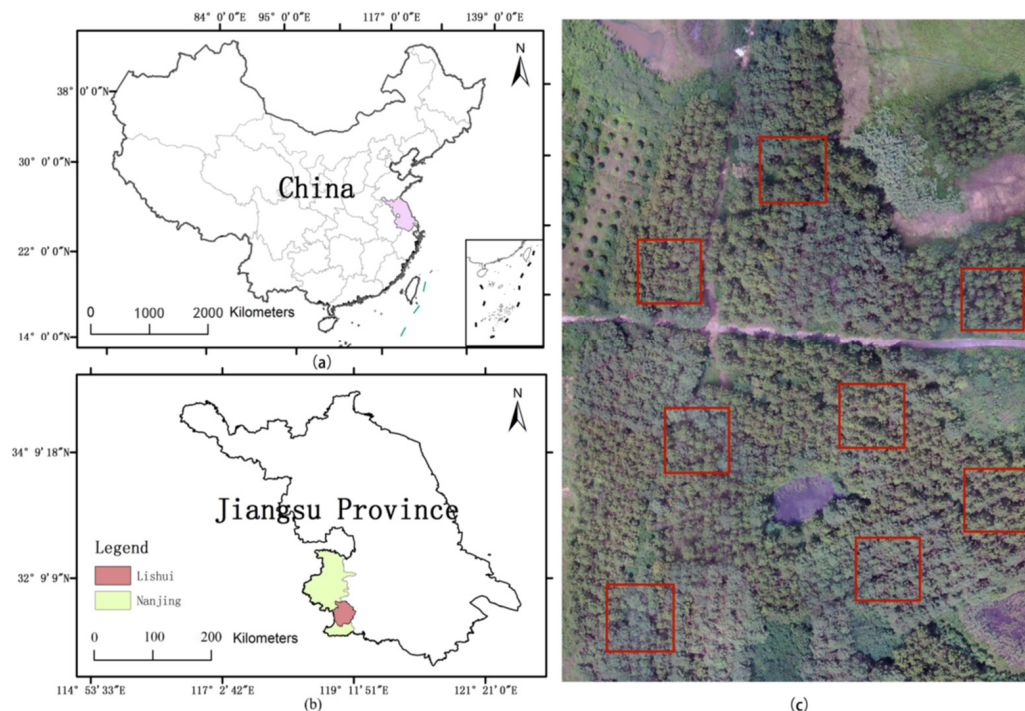


**Figure 1.** (a) Location of the study site within China; (b) location of the study site within Jiangsu province; and (c) the image of the experimental area obtained on 10 July at a 10 cm spatial resolution. Masson pine was the dominant tree species in the study area, with an average age of 30 years and similar tree sizes. The red squares are the plots with sizes of  $30 \times 30$  m which divided the area.

## 2.2. Data Acquisition and Preprocessing

Masson pine (*Pinus massoniana*) was the dominant tree species in this area, with an average tree age of 30 years and similar tree sizes (Table 1). To prevent healthy sample trees from being affected by the PWN-injected sample trees, we divided the area into eight plots with sizes  $30 \times 30$  m, and randomly sampled one tree from each plot (a total of eight sample trees) for further study. Four pine trees that were confirmed to be healthy were manually injected with PWN. The PWNs were obtained from pine trees infected with PWD in another forest of Lishui, Nanjing, Jiangsu province using the Baermann funnel method and proliferated in the laboratory for one week at  $25\text{ }^{\circ}\text{C}$  in the dark. Each pine tree was injected with  $10,000/100\text{ }\mu\text{L}$  of a PWN suspension on 6 July to simulate natural PWN infection [27,28]. The steps of PWN injection were: (1) A 1.0 cm diameter hole was made by drill at breast height, deep enough reach the xylem, but not more than  $1/3$  of the tree diameter at that height. (2) The PWN suspension was injected into the hole using a microsyringe after inserting pasteurized cotton. (3) The tree section with the cotton was wrapped with transparent tape to reduce the loss of the PWN suspension [29]. As a control, another four healthy trees were injected with distilled water without any other treatment. The needles of each sample tree were taken to the laboratory before PWN inoculation and after each UAV data collection survey. The presence of PWN in needles was determined using a microscope according to morphological methods [30]. Finally, after the experiment, the sample trees injected with PWN were cut down and disposed of to prevent the spread of PWD.

**Table 1.** The growth situation of sample trees. There were eight sample trees (H: tree height; DBH: diameter at breast height.).

	Mean	Standard Deviation	Maximum	Minimum	Range
H (m)	15.07	0.77	16.31	13.78	2.53
DBH (cm)	18.17	1.54	20.11	15.68	4.43

During the experiment, continuous monitoring included symptom observations and UAV-based image collection every four days, every week, and every month in the early, mid-, and late infection stages, respectively. Image acquisition flight campaigns were conducted between 10:00 a.m. and 3:00 p.m.; the specific data acquisition time was adjusted according to the weather. Based on the previous studies, this study divided PWD into three stages: (1) early infection stage, (2) mid-infection stage, and (3) late infection stage. Specifically, we defined the early infection stage as the period when PWN infection was confirmed in pine trees by morphological methods but no visual symptoms were apparent. We defined the mid-infection stage as the period when symptoms of needle discoloration and wilting began to be visible to naked eye. We defined the late infection stage as the period when more than 50% needles showed discoloration and wilting. The hyperspectral images obtained on 10 July, 24 August, and 17 October were selected as representative of early, mid-, and late infection stages of PWD, respectively.

The DJI Matrice 600 Pro UAV equipped with the Gaiasky-mini-2 hyperspectral imaging spectrometer (a line scanner) was used to collect hyperspectral images at different spatio-temporal scales (different altitudes at different times). The imaging mode of the GaiaSky-mini spectrometer is a built-in push-sweep model. The imaging lens and the imaging spectrometer are separate. The front end of the imaging spectrometer has its corresponding incident slit (represented by black double arrows), and the red circle (inside) represents the focusing lens at the rear end of the imaging lens. The incident slit has a certain length. When the encounter is blocked by the focusing lens, part of the image will be blocked and the image cannot be acquired normally. Similarly, when the slit position exceeds the termination position, it will also be blocked and the image cannot be acquired. Therefore, the lens calibration can be carried out when the parameter setting is unreasonable or there is an uneven black area at the edge of the captured image. At the same time, the lens is not a plane. In the process of image acquisition, the slit is shot line by line relative to the mirror of the focusing lens, so there will be image distortion in the plane, but it is not very obvious during observation. The lens calibration method can eliminate these drawbacks. This step is completed in batch processing on Specview, the acquisition software. You only need to check the lens calibration parameter file to correct the influence of internal image distortion caused by built-in push and sweep on stitching. The DJI Matrice 600 pro UAV (DJI, ShenZhen, China) provided GPS information using a professional-class A3 pro flight control system with a GNSS module. The horizontal position error of the UAV was  $\pm 1.5$  m and the vertical position error was  $\pm 0.5$  m. The spectrometer samples spanned from 400 nm to 1000 nm and included 176 bands. The field of view (FOV) and instantaneous field of view (IFOV) were  $\geq 36^\circ$  and  $\leq 0.36$  mRad, respectively. To eliminate the error during image collection, some preprocessing was conducted. The image forward and side overlaps were set to 70%, and the lens exposure time was automatically adjusted. Further data calibration was performed in SpecVIEW 2.9.2.31 (Dualix spectral imaging, Nanjing, China) to obtain reflectance products. The reflectance correction and radiometric calibration were conducted using a Barium sulfate calibration panel and a 4 m<sup>2</sup> gray carpet [31]. Finally, images were stitched in Agisoft Photoscan professional 1.4.3 (Agisoft, St. Petersburg, Russia), and the workflow included photo alignment, alignment optimization, generating the dense point cloud, mesh generation, texture generation, and orthophoto export. The heights in this report are given as the flight height relative to the take-off site. The flight height were 50 m, 100 m, 150 m, 200 m, 250 m, and 300 m. The corresponding spatial resolutions were 2 cm, 4 cm, 6 cm, 8 cm, 10 cm, and 12 cm. The spatial resolution conversion formula

provided by the Dualix spectral imaging company was used to obtain the spatial resolution corresponding to flight height. The conversion formula is as follows:

$$SP = WLFV/960 \quad (1)$$

$$WLFV = ((H \times 1000 - F) \times WCCD)/(F \times 1000) \quad (2)$$

where SP, WLFV, WCCD, H, and F represent the spatial resolution, the width of line field of view, the width of CCD, the flight height, and the focal length of the lens, respectively. The 960 was the line number of this camera. The 1000 was used to convert the units.

The canopy pixels of infected and non-infected pine trees were extracted using the region growing algorithm [32] in ENVI 5.3 (Harris Geospatial, Fort Collins, CO, USA). First, the initial growth seeds were selected on the canopy images of each tree to initiate the process and sample the spectral curve. Then the Standard deviation multiplier and neighbor size were set to 1.2 and 8, respectively, which meant that if the Standard deviation multiplier between the neighbor pixels and growth seed were smaller than 1.2, these pixels will be classified as new growth seed. Finally, the pixels stopped growing when there were no pixels remaining in the area that met the growth criteria.

### 2.3. Data Analysis

Jeffries–Matusita (J-M) distance is a spectral separability method based on conditional probability density, which has been widely used in similar object classification applications [33]. In this study, the J-M distance can effectively distinguish diseased and healthy pine samples, and the J-M distance was calculated in MATLAB R2014a (MathWorks, USA) to compare the separability between infected and healthy samples in different bands. The formula is as follows [34]:

$$J_{ij} = \left\{ \int_X [\sqrt{P(X/\omega_i)} - \sqrt{P(X/\omega_j)}]^2 \right\}^{1/2} \quad (3)$$

where  $P(X/w_i)$  is the conditional probability density, that is, the probability that the  $i$ th pixel belongs to the  $w_i$ th category. The value of  $J_{ij}$  ranges between 0 and 2. The larger the value, the higher the separability.

The vegetation indices (VIs) derived from radiometric data have primarily been used to analyze and detect changes in plant biophysical parameters [35,36]. After injection with PWN, the biophysical parameters such as chlorophyll and water content of the infected trees will change, and the VIs can capture and magnify these changes and help distinguish between infected and healthy trees. In this study, eight existing VIs from previous PWD detection research [7,8,18,36] and two modified VIs were calculated according to the characteristic bands with the highest J-M distances (Table 2).

**Table 2.** Algorithm and references of selected vegetation indices.

Vegetation Indices	Equation	Reference
Modified normalized difference vegetation index (mNDVI)	$mNDVI = \frac{R_{777.784} - R_{655.672}}{R_{777.784} + R_{655.672}}$	[37]
Modified ratio vegetation index (mRVI)	$mRVI = \frac{R_{777.784}}{R_{655.672}}$	[38]
Plant senescence reflectance index (PSRI)	$PSRI = \frac{R_{672}}{R_{550} + 3 \cdot R_{708}}$	[11]
Pigment-specific normalized difference (PSND)	$PSND = \frac{R_{800} - R_{680}}{R_{800} + R_{680}}$	[39]
Red edge position (REP)	$REP = 700 + 40 \cdot \frac{R_{re} - R_{700}}{R_{740} + R_{700}}$ $R_{re} = \frac{(R_{670} + R_{780})}{2}$	[40]
Structure insensitive pigment index (SIPI)	$SIPI = \frac{R_{800} - R_{445}}{R_{800} - R_{680}}$	[41]
Normalized Difference 750/705 Chl NDI (NDVI705)	$NDVI705 = \frac{R_{750} - R_{705}}{R_{750} + R_{705}}$	[41]

Table 2. Cont.

Vegetation Indices	Equation	Reference
Pigment specific simple ration of Chl a (PSSRa)	$PSSRa = \frac{R_{800}}{R_{680}}$	[42]
Pigment specific simple ration of Chl b (PSSRb)	$PSSRb = \frac{R_{800}}{R_{635}}$	[42]
Green normalized difference vegetation index (GNDVI)	$GNDVI = \frac{R_{NIR} - R_{green}}{R_{NIR} + R_{green}}$	[43]

The Kruskal–Wallis (K-W) test is a non-parametric method that analyzes whether there are significant differences in the distributions of multiple groups of samples. We performed K-W test on the calculated J-M distances and VI values in SPSS 9.4 (IBM, Stanford, CA, USA) to analyze the impact of different spatiotemporal scales on J-M distances and VIs (Tables 3–5). Moreover, the Bonferroni correction was used to reduce the error. The limit for statistical significance ( $p$ ) was set at 0.05 [44].

Random forest (RF) is a machine learning algorithm composed of multiple decision trees [45]. The main steps of random forest in classification are: (1) the bootstrap method is used to generate random training sets. (2) Randomly sample features from all attributes and select the best split according to a principal such as Gini impurity (the probability of misclassification based on the feature distribution) to establish a decision tree. (3) Repeat the first two steps to establish a large number of decision trees to form a random forest classifier. (4) The prediction targets are classified according to the voting results of each decision tree in the forest [46]. We established the pixel-level PWD detection models using the random forest classifier meta estimator in the scikit-learn machine learning library [47] in Python 3.8.8. The confusion matrix was used to assess the models performance and provide information about the number of pixels (Tables 6–9). All the samples were randomly split into training and testing sets at a 70%/30% ratio, and the decision tree number was set to 500. Moreover, bootstrap was set as True and max\_features was set to auto. Random forest classifiers reflect the importance of features based on their ability to discriminate between target classes; Gini impurity was used to calculate feature importance in this study.

**Table 3.** Significance between groups of J-M distances at different spatial resolutions obtained by using the Kruskal–Wallis test. The limit for statistical significance ( $p$ ) was set at 0.05. The \* represents significant difference. The SP is the spatial resolution.

SP1-SP2	Adj.Sig.	
	Early	Mid
2-4	0.000 *	0.000 *
2-6	0.000 *	0.187
2-8	0.001 *	0.000 *
2-10	0.000	0.000 *
2-12	0.000	0.002 *
4-6	1.000	0.006 *
4-8	0.155	0.051
4-10	0.000 *	1.000
4-12	0.973	1.000
6-8	0.577	0.000 *
6-10	0.000 *	0.001 *
6-12	0.288	1.000
8-10	0.000 *	0.256
8-12	0.000 *	0.000 *
10-12	0.000 *	0.264

**Table 4.** Significance between VIs groups at different spatial resolutions obtained using the Kruskal–Wallis test in the early infection stage. The limit for statistical significance ( $p$ ) was set at 0.05. The \* represents significant difference. The SP is the spatial resolution.

Early Stage		Adj.Sig.								
SP1-SP2	mNDVI	mRVI	PSRI	PSND	REP	SIPI	PSSRa	PSSRb	GNDVI	NDVI705
2-4	0.000 *	0.000 *	0.000 *	0.000 *	0.000 *	0.000 *	0.000 *	0.000 *	0.000 *	0.000 *
2-6	0.089	0.089	0.000 *	1.000	0.000 *	0.000 *	1.000	0.000 *	0.000 *	0.000 *
2-8	0.000 *	0.000 *	0.000 *	0.000 *	0.000 *	0.107	0.000 *	0.000 *	0.000 *	1.000
2-10	0.000 *	0.000 *	0.000 *	0.000 *	0.083	0.003	0.000 *	0.000 *	0.000 *	0.000 *
2-12	0.000 *	0.000 *	0.000 *	0.000 *	0.000 *	0.000 *	0.000 *	0.000 *	0.000 *	0.000 *
4-6	0.000	0.000	0.000	0.000	0.008 *	1.000	0.000	0.000	0.000	0.451
4-8	0.000 *	0.000 *	0.000 *	0.000 *	0.000 *	0.000 *	0.000 *	0.000 *	0.000 *	0.000 *
4-10	0.000 *	0.000 *	0.000 *	0.000 *	0.000 *	0.000 *	0.000 *	0.000 *	0.000 *	0.000 *
4-12	0.000 *	0.000 *	0.000 *	0.000 *	0.000 *	0.000 *	0.000 *	0.000 *	0.000 *	0.000 *
6-8	0.000 *	0.000 *	0.000 *	0.000 *	0.000 *	0.000 *	0.000 *	1.000	0.000 *	0.000 *
6-10	0.000 *	0.000 *	0.000 *	0.000 *	0.000 *	0.000 *	0.000 *	0.000 *	0.000 *	0.000 *
6-12	0.000 *	0.000 *	0.000 *	0.000 *	0.000 *	0.000 *	0.000 *	0.000 *	0.000 *	0.000 *
8-10	0.000 *	0.000 *	0.000 *	0.000 *	0.000 *	0.000 *	0.000 *	0.000 *	0.000 *	0.000 *
8-12	0.000 *	0.000 *	0.000 *	0.000 *	0.000 *	0.000 *	0.000 *	0.000 *	0.000 *	0.000 *
10-12	0.216	0.216	0.751	0.100	0.052	1.000	0.100	0.028 *	0.018 *	0.494

**Table 5.** Significance between VIs groups at different spatial resolutions obtained using the Kruskal–Wallis test in the mid-infection stage. The limit for statistical significance ( $p$ ) was set at 0.05. The \* represents significant difference. The SP is the spatial resolution.

Mid Stage		Adj.Sig.								
SP1-SP2	mNDVI	mRVI	PSRI	PSND	REP	SIPI	PSSRa	PSSRb	GNDVI	NDVI705
2-4	0.000 *	0.000 *	0.000 *	0.000 *	0.000 *	0.000 *	0.000 *	0.000 *	0.000 *	0.000 *
2-6	0.000 *	0.000 *	0.000 *	0.928	0.000 *	0.000 *	0.928	1.000	0.000 *	0.000 *
2-8	1.000	1.000	0.000 *	0.000 *	0.000 *	0.001 *	0.000 *	0.000 *	0.000 *	0.000 *
2-10	1.000	1.000	0.000 *	0.000 *	0.000 *	0.000 *	0.000 *	0.000 *	0.000 *	0.000 *
2-12	1.000	1.000	0.000 *	0.000 *	0.000 *	0.000 *	0.000 *	0.000 *	0.000 *	0.000 *
4-6	0.827	0.827	1.000	0.017 *	0.023 *	0.000 *	0.000 *	0.016 *	0.000 *	0.000 *
4-8	0.000 *	0.000 *	0.000 *	0.000 *	1.000	0.000 *	0.000 *	0.000 *	0.000 *	0.001 *
4-10	0.000 *	0.000 *	0.000 *	0.000 *	1.000	0.000 *	0.000 *	0.000 *	0.000 *	0.054
4-12	0.000 *	0.000 *	0.000 *	0.000 *	1.000	0.000 *	0.000 *	0.000 *	0.000 *	0.052
6-8	0.000 *	0.000 *	0.000 *	0.000 *	1.000	0.000 *	0.000 *	0.000 *	0.000 *	0.000 *
6-10	0.012 *	0.012 *	0.000 *	0.000 *	0.474	0.000 *	0.000 *	0.000 *	0.185	0.543
6-12	0.000 *	0.000 *	0.000 *	0.000 *	0.130	0.000 *	0.000 *	0.000 *	0.000 *	1.000
8-10	1.000	1.000	1.000	1.000	1.000	0.000 *	1.000	1.000	0.000 *	0.000 *
8-12	1.000	1.000	0.000 *	0.035 *	1.000	0.000 *	0.035 *	0.001 *	0.000 *	0.000 *
10-12	1.000	1.000	0.000 *	0.148	1.000	0.004	0.148	0.255	0.087	1.000

**Table 6.** Significance between VIs groups at different spatial resolutions obtained using the Kruskal–Wallis test in the late infection stage. The limit for statistical significance ( $p$ ) was set at 0.05. The \* represents significant difference. The SP is the spatial resolution.

Late Stage		Adj.Sig.								
SP1-SP2	mNDVI	mRVI	PSRI	PSND	REP	SIPI	PSSRa	PSSRb	GNDVI	NDVI705
2-4	0.000 *	0.000 *	0.000 *	0.000 *	1.000	0.000 *	0.000 *	0.035 *	0.000 *	1.000
2-6	0.000 *	0.000 *	0.000 *	0.000 *	0.000 *	0.000 *	0.000 *	0.000 *	0.000 *	0.000 *
2-8	0.000 *	0.000 *	0.000 *	0.000 *	0.000 *	0.000 *	0.000 *	0.000 *	0.000 *	0.000 *
2-10	0.000 *	0.000 *	0.000 *	0.000 *	0.000 *	0.000 *	0.000 *	0.000 *	0.000 *	0.000 *
2-12	1.000	1.000	0.012 *	0.908	1.000	0.070	0.908	0.000 *	0.000 *	0.000 *

Table 6. Cont.

Late Stage	Adj.Sig.										
	SP1-SP2	mNDVI	mRVI	PSRI	PSND	REP	SIPI	PSSRa	PSSRb	GNDVI	NDVI705
4-6	0.008 *	0.008 *	0.002 *	0.060 *	0.000 *	0.000 *	0.000 *	0.060	0.315	0.382	0.138
4-8	0.000 *	0.000 *	0.000 *	0.000 *	0.000 *	0.000 *	0.000 *	0.000 *	0.000 *	0.000 *	0.000 *
4-10	0.000 *	0.000 *	0.000 *	0.000 *	0.000 *	0.000 *	0.000 *	0.000 *	0.093	0.000 *	0.000 *
4-12	0.493	0.493	1.000	0.003 *	1.000	1.000	0.003 *	0.000 *	0.000 *	0.000 *	0.000 *
6-8	0.000 *	0.000 *	0.000 *	0.000 *	0.992	0.000 *	0.000 *	0.048 *	0.000 *	0.000 *	0.836
6-10	0.000 *	0.000 *	0.000 *	0.003 *	0.006 *	0.000 *	0.003 *	1.000	0.000 *	0.000 *	0.000 *
6-12	0.002 *	0.002 *	0.325	0.000 *	1.000	0.318	0.000 *	0.000 *	0.001 *	0.000 *	0.000 *
8-10	1.000	1.000	1.000	1.000	0.826	0.096	1.000	1.000	0.000 *	0.000 *	0.000 *
8-12	0.000 *	0.000 *	0.000 *	0.000 *	0.062	0.000 *	0.000 *	0.000 *	0.000 *	1.000	0.000 *
10-12	0.000 *	0.000 *	0.000 *	0.000 *	0.001 *	0.000 *	0.000 *	0.000 *	0.000 *	0.000 *	1.000

**Table 7.** The confusion matrix of the random forest-based PWD detection model on 10 July (early infection stage). The pixels extracted from the canopy were classified. The SP represents the spatial resolution. UA: user's accuracy; PA: producer's accuracy; OA: overall accuracy.

10 July				
SP: 2 cm	Infected	Healthy	Total	UA (%)
Infected	2351	883	3234	72.69
Healthy	809	2493	3302	75.49
Total	3160	3376	6536	Kappa: 0.48
PA (%)	74.39	73.84		OA (%): 74.11
SP: 4 cm	Infected	Healthy	Total	UA (%)
Infected	681	292	973	69.99
Healthy	220	775	995	77.89
Total	901	1067	1968	Kappa: 0.48
PA (%)	75.58	72.63		OA (%): 73.98
SP: 6 cm	Infected	Healthy	Total	UA (%)
Infected	372	152	524	70.99
Healthy	130	355	485	73.20
Total	502	507	1009	Kappa: 0.44
PA (%)	74.10	70.02		OA (%): 72.05
SP: 8 cm	Infected	Healthy	Total	UA (%)
Infected	206	60	266	77.44
Healthy	58	210	268	78.36
Total	264	270	534	Kappa: 0.56
PA (%)	78.03	77.78		OA (%): 77.90
SP: 10 cm	Infected	Healthy	Total	UA (%)
Infected	182	52	234	77.78
Healthy	42	182	224	81.25
Total	224	234	458	Kappa: 0.59
PA (%)	81.25	77.78		OA (%): 79.48
SP: 12 cm	Infected	Healthy	Total	UA (%)
Infected	113	34	147	76.87
Healthy	40	112	152	73.68
Total	153	146	299	Kappa: 0.51
PA (%)	73.86	76.71		Overall accuracy: 75.25

**Table 8.** The confusion matrix of the random forest-based PWD detection model on 24 August (mid-infection stage). The pixels extracted from the canopy were classified. The SP represents the spatial resolution. UA: user’s accuracy; PA: producer’s accuracy; OA: overall accuracy.

24 August				
SP: 2 cm	Infected	Healthy	Total	UA (%)
Infected	3046	699	3745	81.34
Healthy	172	3507	3679	95.32
Total	3218	4206	7424	Kappa: 0.77
PA (%)	94.66	83.38		OA (%): 88.27
SP: 4 cm	Infected	Healthy	Total	UA (%)
Infected	991	305	1296	76.47
Healthy	74	1309	1383	94.65
Total	1065	1614	2679	Kappa: 0.72
PA (%)	93.05	81.10		OA (%): 85.85
SP: 6 cm	Infected	Healthy	Total	UA (%)
Infected	524	150	674	77.74
Healthy	42	578	620	93.23
Total	566	728	1294	Kappa: 0.70
PA (%)	92.58	79.39		OA (%): 85.16
SP: 8 cm	Infected	Healthy	Total	UA (%)
Infected	340	56	396	85.86
Healthy	27	375	402	93.28
Total	367	431	798	Kappa: 0.80
PA (%)	92.64	87.01		OA (%): 89.59
SP: 10 cm	Infected	Healthy	Total	UA (%)
Infected	213	48	261	81.61
Healthy	19	221	240	92.08
Total	232	269	501	Kappa: 0.73
PA (%)	91.81	82.16		OA (%): 86.63
SP: 12 cm	Infected	Healthy	Total	UA (%)
Infected	155	36	191	81.15
Healthy	22	143	165	86.67
Total	177	179	356	Kappa: 0.67
PA (%)	87.57	79.89		OA (%): 83.71

**Table 9.** The confusion matrix of the random forest-based PWD detection model on 17 October (late infection stage). The pixels extracted from the canopy were classified. The SP represents the spatial resolution. UA: user’s accuracy; PA: producer’s accuracy; OA: overall accuracy.

17 October				
SP: 2 cm	Infected	Healthy	Total	UA (%)
Infected	3092	57	3149	98.19
Healthy	35	2473	2508	98.60
Total	3127	2530	5657	Kappa: 0.97
PA (%)	98.88	97.75		OA (%): 98.37
SP: 4 cm	Infected	Healthy	Total	UA (%)
Infected	1309	15	1324	98.87
Healthy	2	1024	1026	99.81
Total	1311	1039	2350	Kappa: 0.98
PA (%)	99.85	98.56		OA (%): 99.28
SP: 6 cm	Infected	Healthy	Total	UA (%)
Infected	616	13	629	97.93
Healthy	6	437	443	98.65
Total	622	450	1072	Kappa: 0.96
PA (%)	99.04	97.11		OA (%): 98.23

Table 9. Cont.

17 October				
SP: 8 cm	Infected	Healthy	Total	UA (%)
Infected	393	8	401	98.00
Healthy	5	241	246	97.97
Total	398	249	642	Kappa: 0.97
PA (%)	98.74	96.79		OA (%): 98.75
SP: 10 cm	Infected	Healthy	Total	UA (%)
Infected	208	11	219	94.98
Healthy	2	187	189	98.94
Total	210	198	408	Kappa: 0.94
PA (%)	99.05	94.44		OA (%): 96.81
SP: 12 cm	Infected	Healthy	Total	UA (%)
Infected	135	3	138	97.83
Healthy	4	138	142	97.18
Total	139	141	280	Kappa: 0.95
PA (%)	97.12	97.87		OA (%): 97.50

### 3. Results

#### 3.1. Spectral Responses in Different PWD Infection Stages

The spectral reflectance curves of the infected trees changed significantly over time (Figure 2). In the early infection stage (10 July), the vegetation spectra exhibited typical characteristics such as the red band absorption valley (red valley) and the green band reflectance peak (green peak). The reflectance of these bands was highly correlated with plant infection status. In the mid-infection stage (24 August), the reflectance in the “red valley” had significantly increased, which indicated the plant had been attacked by PWN. As the PWD developed, the “green peak” and “red valley” gradually disappeared. In the late infection stage (17 October), they had disappeared entirely and the spectral curve in visible region became a straight line. The reflectance in near infra-red (NIR), which is highly related with water content, was much lower in the late infection stage than other infection stages. In this infection stage, the needles showed visible discoloration and wilting (Figure 3).

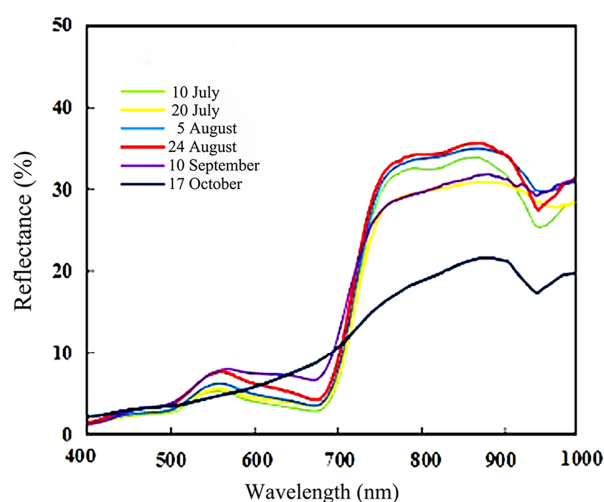


**Figure 2.** The spectral reflectance curves of infected samples at different infection stages. Typical vegetation spectral characteristics such as the red band absorption valley (red valley) and green band reflectance peak (green peak) were apparent on 10 July, but gradually disappeared with the PWD development.



**Figure 3.** The images of pine canopy from different PWD-infection stages.

### 3.2. Analysis of the Impact of Spatio-Temporal Scale on the Spectral Separability

In the early infection stage, the J-M distances across all wavelengths were higher than 1.48 and lower than 1.60 (Figure 4a). In the visible region, there were two obvious J-M distance peaks with maximum values in the ranges of 401–420 nm (1.59) and 655–672 nm (1.52), respectively. J-M distances higher than 1.50 indicated there was separability between infected and non-infected samples. Furthermore, the J-M distance in the green region was lower than the other wavelengths in the visible region. Although the J-M distance in the near infrared region was higher than 1.5, the fluctuation was smaller than that in visible region. With the increase in the wavelength, the J-M distance rose slowly and peaked within 902–924 nm (1.56). In the red edge region, as the wavelength increased, the J-M distance first decreased and then increased rapidly. According to the significance calculated by Kruskal–Wallis test at different spatial resolutions (Table 3), except for five comparable groups: 4 cm and 6 cm, 4 cm and 8 cm, 4 cm and 12 cm, 6 cm and 8 cm and, 6 cm and 12 cm, the other ten groups showed significant differences ( $p \leq 0.05$ ). Furthermore, the difference of separability between the 4 cm and 6 cm spatial resolutions was the least significant ( $p = 1$ ).

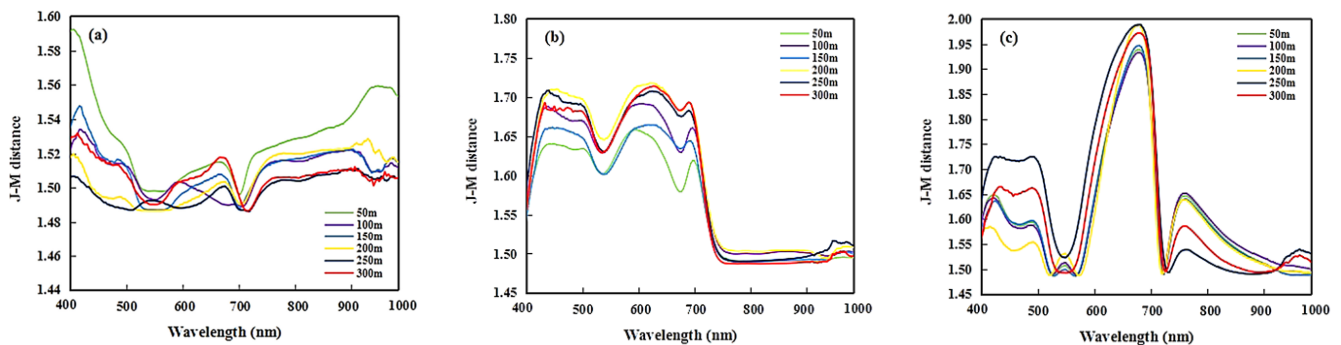


**Figure 4.** Panels (a–c) show the J-M distance curves obtained at different spatial resolutions in the early, mid-, and late infection stages, respectively. The J-M distance curves show the J-M distance values at different bands. The J-M distances ranged between 0–2.

In the mid-infection stage, the J-M distances across all the wavelengths were higher than 1.48 and lower than 1.72 (Figure 4b). The difference and the highest value were 0.24 and 1.72, respectively, both of which were 0.12 higher than those in the early infection stage. In the visible region, there were two obvious J-M distance peaks that had maximum values in the 423–443 nm (1.71) and 594–621 nm (1.72) ranges, respectively. The J-M distance of the green region was smaller than those of other wavelengths in visible region. In the red edge region, the J-M distance increased initially and then decreased rapidly with increasing wavelength. The J-M distances in the near infrared region fluctuated slightly around 1.50 and were much lower than those in visible region. In addition to the seven groups: 2 cm and 6 cm, 4 cm and 8 cm, 4 cm and 10 cm, 4 cm and 12 cm, 6 cm and 12 cm, 8 cm and 10 cm,

and 10 cm and 12 cm, the other eight groups showed significance differences ( $p \leq 0.05$ ). In addition, the 4 cm and 10 cm, 4 cm and 12 cm, and 6 cm and 12 cm groups were the least significant ( $p = 1$ ) (Table 3).

In the late infection stage, the J-M distances across all wavelengths were higher than 1.48 and lower than 1.99 (Figure 4c). The difference between the minimum and maximum was 0.52, which was much higher than the early and mid-infection stages. The highest J-M distance approached 2, which represented the highest separability observed during the experiment. The difference in the highest values of the late infection stage and mid-infection stage was 0.27, which was larger than the difference between the early and mid-infection stages. In the visible region, there were two obvious J-M distance peaks and the maximum values occurred between 417–430 nm (1.73) and 669–679 nm (1.98), respectively. Specifically, the J-M distances in the range of 669–679 nm were higher than 1.90 at different spatial resolutions, which indicated high separability. Furthermore, the J-M distance in the green region was lower than other wavelengths in the visible region. In the red edge region, the J-M distance decreased rapidly with the increasing wavelength. In the near infrared region, there was an obvious J-M peak with a maximum value at 755–766 nm (1.65). However, the asymptotic significance (2-sided tests) of J-M distance at different spatial resolutions in late infection stages was 0.214 ( $p > 0.05$ ), which indicated there were no significant differences between groups (Table 3).

### 3.3. Analysis of the Impact of Spatio-Temporal Scale on Vegetation Indices

In the early infection stage, except for green normalized difference vegetation index (GNDVI), all VIs were significantly affected by spatial resolution. Most of the VIs were significantly different between the 10 cm and 12 cm spatial resolutions. The structure intensive pigment index (SIPI) and normalized difference vegetation index 705 (NDVI705) were more susceptible to changes in spatial resolution than other VIs (Table 4). In the mid-infection stage, in addition to SIPI, all VIs showed significant differences between different spatial resolutions. The red edge position (REP), mNDVI, and mRVI were more likely to be affected by changes in spatial resolutions. All VIs showed significant differences between 2 cm and 4 cm spatial resolutions in both early and mid-infection stages (Table 5). In the late infection stage, all the VIs were significantly affected by changes in spatial resolutions. Most of them showed large differences between the 8 cm and 10 cm spatial resolutions. REP was most susceptible to changes in spatial resolution, but the pigment specific normalized difference (PSND) and GNDVI were least affected (Table 6).

### 3.4. PWD Detection Accuracy and Feature Importance

The model accuracy was higher than 70% in the three infection stages (Figure 5). In the early infection stage, the PWD detection accuracy was higher than 72% and lower than 80% at all spatial resolutions. The accuracy of 8 cm and 10 cm spatial resolutions was higher than those of other spatial resolutions and the peak accuracy occurred at the 10 cm spatial resolution (overall accuracy (OA%): 79.48%, Kappa: 0.59) (Figure 6). The difference between the maximum and minimum was 7.43%. Both the producer's accuracy (PA) and the user's accuracy (UA) were best at a spatial resolution of 10 cm. The PA and UA of the infected samples were the same as those of the healthy samples, 81.25% and 77.78% (Table 7). In the mid-infection stage, the PWD detection accuracy at different spatial resolutions were all higher than 83% and lower than 90%. The difference between the maximum and minimum accuracy of different resolutions was 5.88%. In addition, the accuracy at the 8 cm and 2 cm spatial resolutions was higher than other spatial resolutions, and the 8 cm spatial resolution had the highest accuracy (OA%: 89.59%, Kappa: 0.80). The PA of infected and healthy samples was the highest at 2 cm (94.66%) and 8 cm (87.01%) spatial resolutions, respectively. The UA of infected and healthy samples was the highest at the 8 cm spatial resolution (81.34% and 95.32%). In addition, the PA of infected samples was significantly higher than those of the healthy samples, and the UA of healthy samples was much higher than those of the infected samples (Table 8). In the late infection stage, the

PWD detection accuracy at different spatial resolutions was all higher than 95%. However, there was a small fluctuation and a slight decrease between 10 cm and 12 cm spatial resolutions. The 4 cm and 10 cm spatial resolutions had the maximum (OA%: 99.28%, Kappa: 0.98) and minimum (OA%: 96.81%, Kappa: 0.94) accuracy, respectively. Both the PA and UA of infected and healthy samples were highest at the 4 cm spatial resolution (Table 9).

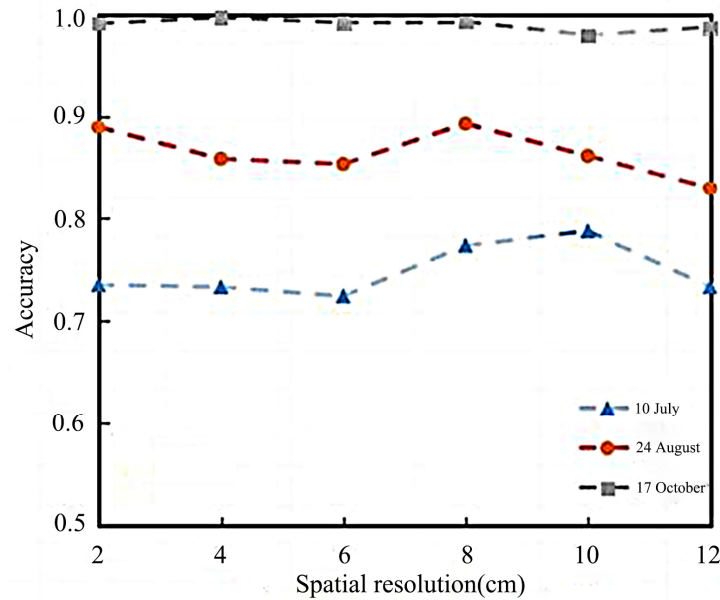


**Figure 5.** The classification accuracy of the PWD detection model established using the random forest algorithm and vegetation indices at different spatio-temporal scales. The blue, orange, and gray dashed lines indicate the changes in accuracy of the PWD detection model at different spatial resolutions in the early (10 July), mid- (24 August), and late (17 October) stages of PWD, respectively. The accuracy increased as the PWD developed.

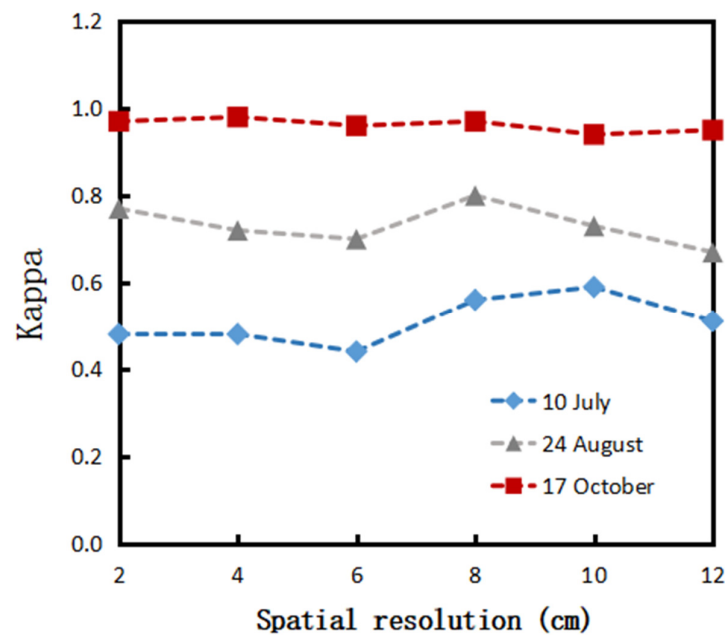


**Figure 6.** The Kappa of the PWD detection model established using the random forest algorithm and vegetation indices at different spatio-temporal scales. The blue, gray and red dashed lines indicate the changes in accuracy of the PWD detection model at different spatial resolutions in the early (10 July), mid- (24 August), and late (17 October) stages of PWD, respectively.

The Gini index was used to calculate the importance of different VIs, i.e., the model features to the PWD detection models (Figure 7). In the early infection stage (Figure 7a), the GNDVI and REP showed more contributions than other VIs. By comparing the feature importance of different VIs at different spatial resolutions it was found that the importance of GNDVI was higher than other VIs at 2 cm, 4 cm, 6 cm, and 8 cm spatial resolutions, and the importance of REP was higher than other VIs at 10 cm and 12 cm spatial resolutions. In addition, the plant senescence reflectance index (PSRI), SIPI, REP, GNDVI, and NDVI705 were most important at 10 cm, 2 cm, 10 cm and 12 cm, 4 cm and 6 cm, and 2 cm and 10 cm, respectively.

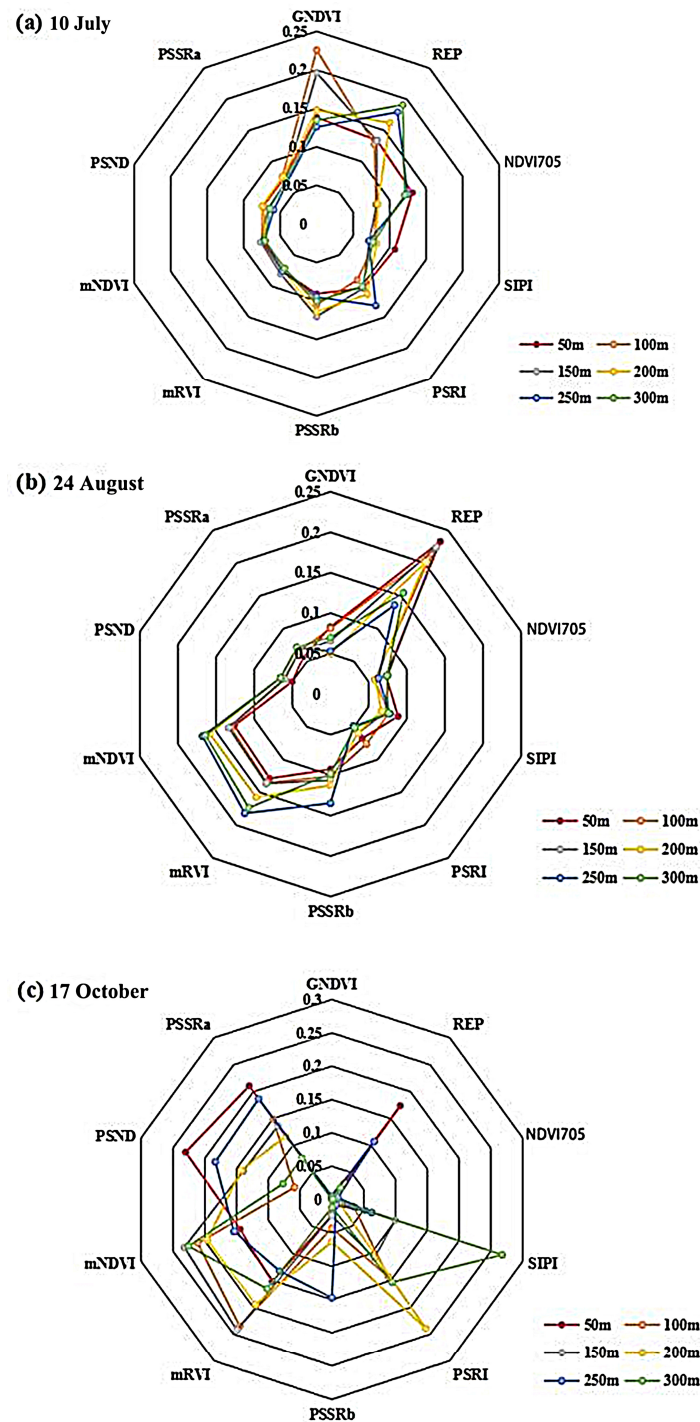


**Figure 7.** (a) The feature importance of different VIs under different spatio-temporal scales in the early infection stage (10 July); (b) the mid-infection stage (24 August); and (c) the late infection stage (17 October).

In the mid-infection stage (Figure 7b), the mNDVI, mRVI, and REP made larger contributions than other VIs. As the spatial resolution decreased, the importance of mNDVI and mRVI increased and REP decreased. The REP had the largest contribution at 2 cm, 4 cm, 6 cm, and 8 cm spatial resolutions. The mRVI had the largest contribution at 10 cm and 12 cm spatial resolutions.

In the late infection stage (Figure 7c), the mNDVI, mRVI, and PSSRa had high importance at most spatial resolutions. However, the GNDVI and NDVI705 made only small contributions at all spatial resolutions. In addition, the VIs that made the largest contribution at different spatial resolutions were also different. At the 2 cm spatial resolution, the pigment specific simple ratio (chlorophyll b) (PSSRb) had the highest importance; at the 4 cm and 6 cm spatial resolutions, the mRVI had the highest importance; at the 8 cm spatial resolution, the PSRI had the highest importance; at the 10 cm spatial resolution, the pigment specific simple ratio (chlorophyll a) (PSSRa) had the highest importance; and at the 12 cm spatial resolution, the SIPI had the highest importance.

#### 4. Discussion

As the PWD develops, the J-M distance of wavelengths to detect PWD increased. Moreover, this study found that the 401–430 nm, 614–624 nm, 655–679 nm, and 755–766 nm wavelengths had better separability than other wavelength regions in PWD detection. These wavelength regions are located in the blue, red, and red edge regions. Similarly, Iordache et al. also identified the 400 nm and 670 nm wavelengths as suitable for PWD detection, and their proposed 750 nm was close to the 755–766 nm observed in this study [8]. Because of the small change in the near infrared region, there were no selected wavelengths in that region. In addition, any data redundancy in the hyperspectral imagery will increase the costs of data processing during practical applications. This can be addressed by programming the camera to scan only the characteristic bands with high J-M distances identified in this study. A wavelength specific camera would greatly simplify data processing and reduce costs.

We selected eight existing VIs and two modified VIs to create a random forest-based PWD detection model which showed high detection accuracy in the early (72.05–79.48%), mid- (83.71–89.59%), and late infection stages (96.81–99.28%). However, the random forest is not a trustworthy machine learning algorithm for variable importance. Compared with manually extracted shallow features, deep learning can automatically explore higher-dimensional information and features of hyperspectral images, which will be useful for future research seeking to improve the early detection of PWD. Indeed, there have been many studies using deep learning for PWD detection [17,48,49].

Outbreaks of PWD in Nanjing, China usually occur from 6 June to 17 October each year. To obtain hyperspectral data of different infection stages, we manually inoculated Masson pine with PWN to simulate the natural infection by PWN and the development of PWD. Considering the strong spread ability of PWD, we only selected four sample trees for PWN inoculation to prevent the uninfected local coniferous forests from acquiring the PWD disease inoculated by this experiment. In addition, more attention should be paid to the influence of other factors such as tree species, terrain, and background on detection.

The optimal spatial resolution for PWD detection increased as PWD developed. In this study, the 10 cm, 8 cm, and 4 cm spatial resolutions were selected as the optimal spatial resolution in early, mid-, and late infection stages, respectively. In the early infection stage, the PWD detection accuracy was low and susceptible to influence from similar objects. Increases in spatial resolution at this stage did not effectively improve the PWD detection accuracy. However, in the mid- and late infection stages, the differences between infected and non-infected samples became more obvious, and higher spatial resolutions made it easier to capture these differences. While the highest spatial resolution in our research was 2 cm, it did not have the highest accuracy for any PWD infection stage, which may have been related to the canopy size of infected trees. Jonathan et al. and Guo et al. also produced similar results [24,25]. Limited by the permitted flying height in the study area, we were only able to collect hyperspectral images below 300 m. Future work should obtain

a larger variety of hyperspectral images containing different canopy sizes to explore the impact of canopy size on the selection of optimal spatial resolution in PWD detection, especially in the early infection stage before symptoms are visible.

## 5. Conclusions

The UAV-based hyperspectral images collected at different infection stages and at different spatial resolutions were used to assess the impact of spatio-temporal scales on PWD detection. The following results were obtained. (1) The separability in the visible region was higher than that of near infrared and red edge regions at different spatio-temporal scales. There was a valley in the J-M distance in the green region and two J-M distance peaks in blue and red regions. The J-M distances at the lower spatial resolutions (8 cm, 10 cm, and 12 cm) were smaller than those of higher spatial resolutions (2 cm, 4 cm, and 6 cm) in the early infection stage, but greater in the mid-infection stage. In the late infection stage, the J-M distances of higher spatial resolutions were greater than those of lower spatial resolutions in near infrared region, but smaller in the visible region. (2) The PWD detection accuracies were 72.05–79.48%, 83.71–89.59%, and 96.81–99.28% with peak accuracies at 10 cm, 8 cm, and 4 cm spatial resolutions during the early, mid-, and late infection stages, respectively. (3) The GNDVI and REP were confirmed as the optimal VIs in early and mid-infection stages, respectively. However, in late infection stage, most VIs had high feature importance, so there was no optimal VI. This research focused on the impact of spatial-temporal scale on PWD detection, and has provided new ideas for future studies. This will play an important role in improving the effectiveness of early PWD detection. Identifying the optimal VIs for PWD detection will help in reducing the loss of forest resources caused by PWD. To apply these results at a larger scale, future research should pay more attention to the impact of other tree species, terrain, and background on forest disease detection.

**Author Contributions:** Conceptualization, J.P. and T.X.; methodology, J.L. and J.P.; software, T.X.; validation, J.L.; formal analysis, J.L. and T.X.; investigation, J.L.; resources, J.P.; data curation, J.P.; writing—original draft preparation, J.P. and J.L.; writing—review and editing, J.P. and J.L.; visualization, J.P. and J.L.; supervision, J.P.; project administration, J.P.; funding acquisition, J.P. All authors have read and agreed to the published version of the manuscript.

**Funding:** This work was supported by the Jiangsu Forestry Science and Technology Innovation and Promotion Project (LYKJ[2021]14) and the National Natural Science Foundation of China (No. 31470579).

**Data Availability Statement:** The data underlying this article will be shared on reasonable request to the corresponding author.

**Conflicts of Interest:** The authors declare no conflict of interest.

## References

1. Gao, R.H.; Shi, J.; Huang, R.; Wang, Z.; Luo, Y. Effects of pine wilt disease invasion on soil properties and Masson pine forest communities in the Three Gorges reservoir region. *China. Ecol. Evol.* **2015**, *5*, 1702–1716. [[CrossRef](#)] [[PubMed](#)]
2. Futai, K. Pinewood Nematode, *Bursaphelenchus xylophilus*. *Annu. Rev. Phytopathol.* **2013**, *51*, 61–83. [[CrossRef](#)] [[PubMed](#)]
3. Shin, H.; Lee, H.; Woo, K.S. Identification of genes up regulated by pine wood nematode inoculation in Japanese red pine. *Tree Physiol.* **2009**, *29*, 411–421. [[CrossRef](#)]
4. Cheng, H.R.; Lin, M.S.; Li, W.Q.; Fang, Z.D. Wilting nematode disease on black pine in Nanjing. *For. Pest Dis.* **1983**, *4*, 1–5.
5. Gao, R.; Wang, Z.; Wang, H.; Hao, Y.; Shi, J. Relationship between Pine Wilt Disease Outbreaks and Climatic Variables in the Three Gorges Reservoir Region. *Forests* **2019**, *10*, 816. [[CrossRef](#)]
6. Ye, J.R.; Wu, X.Q. Research progress of pine wilt disease. *For. Pest Dis.* **2022**, *41*, 1–10.
7. Kim, S.-R.; Lee, W.-K.; Lim, C.-H.; Kim, M.; Kafatos, M.C.; Lee, S.-H.; Lee, S.-S. Hyperspectral Analysis of Pine Wilt Disease to Determine an Optimal Detection Index. *Forests* **2018**, *9*, 115. [[CrossRef](#)]
8. Iordache, M.-D.; Mantas, V.; Baltazar, E.; Pauly, K.; Lewycky, N. A Machine Learning Approach to Detecting Pine Wilt Disease Using Airborne Spectral Imagery. *Remote Sens.* **2020**, *12*, 2280. [[CrossRef](#)]
9. Kozov, N.S.; Osorio, D.T.; Osorio, J.G. Application of remote sensing for monitoring of flood areas. *RUDN J. Eng. Res.* **2019**, *20*, 66–78.

10. Bai, X.Y.; Du, P.J.; Guo, S.C.; Zhang, P. Monitoring Land Cover Change and Disturbance of the Mount Wutai World Cultural Landscape Heritage Protected Area, Based on Remote Sensing Time-Series Images from 1987 to 2018. *Remote Sens.* **2019**, *11*, 1332. [[CrossRef](#)]
11. Merzlyak, M.N.; Gitelson, A.A.; Chivkunova, O.B.; Rakitin, V.Y. Non-destructive optical detection of pigment changes during leaf senescence and fruit ripening. *Physiol. Plant.* **1999**, *106*, 135–141. [[CrossRef](#)]
12. Liu, D.S.; Kelly, G. A spatial-temporal approach to monitoring forest disease spread using multi-temporal high spatial resolution imagery. *Remote Sens. Environ.* **2006**, *101*, 167–180. [[CrossRef](#)]
13. Oerke, E.C. Remote Sensing of Diseases. *Annu. Rev. Phytopathol.* **2020**, *58*, 225–252. [[CrossRef](#)]
14. Li, W.Z.; Shen, S.G.; He, P.; Hao, D.J.; Fang, Y.; Tao, L.; Zhang, S.F. A precisely positioning technique by remote sensing the dead trees in stands with inexpensive small UAV. *J. For. Eng.* **2014**, *28*, 102–106.
15. Zhang, B.; Ye, H.; Lu, W.; Huang, W.; Wu, B.; Hao, Z.; Sun, H. A spatio-temporal Change Detection Method for Monitoring Pine Wilt Disease in a Complex Landscape Using High-Resolution Remote Sensing Imagery. *Remote Sens.* **2021**, *13*, 2083. [[CrossRef](#)]
16. Zhang, S.L.; Huang, J.L.; Hanan, J.; Qin, L. A hyperspectral GA-PLSR model for prediction of pine wilt disease. *Multimed. Tools Appl.* **2020**, *79*, 16645–16661. [[CrossRef](#)]
17. Xu, X.L.; TAO, H.; Li, C.J.; Cheng, C.; Guo, H.; Zhou, J.P. Detection and location of pine wilt disease induced dead pine trees using UAV and deep learning. *Trans. Chin. Soc. Agric. Mach.* **2020**, *51*, 228–236.
18. Yu, R.; Ren, L.L.; Luo, Y.Q. Early detection of pine wilt disease in *Pinus tabulaeformis* in North China using a field portable spectrometer and UAV-based hyperspectral imagery. *For. Ecosyst.* **2021**, *8*, 44. [[CrossRef](#)]
19. Bhardwaj, A.; Sam, L.; Martín-Torres, F.J.; Kumar, R. UAVs as remote sensing platform in glaciology: Present applications and future prospects. *Remote Sens. Environ.* **2016**, *175*, 196–204. [[CrossRef](#)]
20. Su, J.Y.; Liu, C.J.; Hu, X.P.; Xu, X.M.; Guo, L.; Chen, W.-H. Spatio-temporal monitoring of wheat yellow rust using UAV multispectral imagery, Recent Advances in Unmanned Aerial Vehicles Forest Remote Sensing—A Systematic Review. Part II: Research Applications. *Comput. Electron. Agric.* **2019**, *167*, 105035. [[CrossRef](#)]
21. Syifa, M.; Sung, J.P.; Lee, C.W. Detection of the Pine Wilt Disease Tree Candidates for Drone Remote Sensing Using Artificial Intelligence Techniques. *Engineering* **2020**, *6*, 919–926. [[CrossRef](#)]
22. Zhou, X.; Liao, L.; Cheng, D.; Chen, X.; Huang, Q. *Extraction of the Individual Tree Infected by Pine Wilt Disease Using Unmanned Aerial Vehicle Optical Imagery*; ISPRS-International Archives of the Photogrammetry, Remote Sensing and Spatial Information Sciences: Hannover, Germany, 2020; pp. 247–252.
23. Deng, X.L.; Tong, Z.J.; Lan, Y.B.; Huang, Z.X. Detection and Location of Dead Trees with Pine Wilt Disease Based on Deep Learning and UAV Remote Sensing. *AgriEngineering* **2020**, *2*, 294–307. [[CrossRef](#)]
24. Guo, A.; Huang, W.; Dong, Y.; Ye, H.; Ma, H.; Liu, B.; Wu, W.; Ren, Y.; Ruan, C.; Geng, Y. Wheat Yellow Rust Detection Using UAV-Based Hyperspectral Technology. *Remote Sens.* **2021**, *13*, 123. [[CrossRef](#)]
25. Jonathan, P.D.; Michael, S.W.; Grant, D.P.; Marie, H.; Heidi, S.D. Assessing very high resolution UAV imagery for monitoring forest health during a simulated disease outbreak. *ISPRS J. Photogramm. Remote Sens.* **2017**, *131*, 1–14.
26. Zeng, Q.; Sun, H.F.; Yang, Y.L.; Zhou, J.H.; Yang, C. Precision comparison for pine wood nematode disease monitoring by UAV. *J. Sichuan For. Sci. Technol.* **2019**, *40*, 92–95.
27. Ayoub, S.M. *Plant Nematology, an Agricultural Training Aid*; Nema Aid Publications: Sacramento, CA, USA, 1980.
28. Ju, Y.W.; Pan, J.; Wang, X.T.; Zhang, H. Detection of *Bursaphelenchus xylophilus* infection in *Pinus massoniana* from hyperspectral data. *Nematology* **2014**, *16*, 1197–1207. [[CrossRef](#)]
29. Chen, F.M.; Shi, Y.M.; Wang, S.Y.; Tang, J.; Sun, C.Y.; Ye, J.R. Pathogenicity of Different Isolates of *Bursaphelenchus mucronatus* to *Pinus taiwanensis* and *P. thunbergii* Seedlings. *Sci. Silvae Sin.* **2010**, *12*, 86–90.
30. Braasch, H.; Burgermeister, W.; Gu, J. Revised intra-generic grouping of *Bursaphelenchus* Fuchs, 1937 (Nematoda: Aphelenchoidea). *J. Nematode Morphol. Syst.* **2009**, *12*, 65–88.
31. Yu, R.; Luo, Y.Q.; Li, H.N.; Yang, L.Y.; Huang, H.G.; Yu, L.F.; Ren, L.L. Three-Dimensional Convolutional Neural Network Model for Early Detection of Pine Wilt Disease Using UAV-Based Hyperspectral Images. *Remote Sens.* **2021**, *13*, 4065. [[CrossRef](#)]
32. Wang, S.Y.; Higgins, W.E. Symmetric region growing. *IEEE Trans. Image Process.* **2003**, *12*, 1007–1015.
33. Wang, C.X.; Ma, N.; Ming, Y.F.; Wang, Q.; Xia, J.F. Classification of hyperspectral imagery with a 3D convolutional neural network and J-M distance. *Adv. Space Res.* **2019**, *64*, 886–899. [[CrossRef](#)]
34. Tong, Q.X.; Zhang, b.; Zhen, L.F. *Hyperspectral Remote Sensing: Principle, Technology and Application*, 1st ed.; Higher Education Press: Beijing, China, 2006; pp. 135–136.
35. Guo, N. Vegetation Index and Its Advances. *Arid. Meteorol.* **2003**, *4*, 71–75.
36. Mahlein, A.K.; Rumpf, T.; Welke, P.; Dehne, H.-W.; Plümer, L.; Steiner, U.; Oerke, E.-C. Development of spectral indices for detecting and identifying plant diseases. *Remote Sens. Environ.* **2013**, *128*, 21–30. [[CrossRef](#)]
37. Rouse, J.W.; Haas, R.H.; Schell, J.A.; Deering, D.W. Monitoring vegetation systems in the Great Plains with ERTS. In Proceedings of the Third ERTS Symposium, Washington, DC, USA, 10–14 December 1973; pp. 309–317.
38. Jordan, C.F. Derivation of Leaf-Area Index from Quality of Light on the Forest Floor. *Ecology* **1969**, *50*, 663–666. [[CrossRef](#)]
39. Chappelle, E.W.; Kim, M.S.; McMurtrey, J.E., III. Ratio analysis of reflectance spectra (RARS): An algorithm for the remote estimation of the concentrations of chlorophyll A, chlorophyll B and the carotenoid in soybean leaves. *Remote Sens. Environ.* **1992**, *39*, 239–247. [[CrossRef](#)]

40. Guyot, G.; Baret, F. High spectral resolution: Determination of spectral shifts between the red and the near infrared. In Proceedings of the ISPRS Congress, Kyoto, Japan, 1–10 July 1988.
41. Penuelas, J.; Baret, F.; Filella, I. Semi-empirical indices to assess carotenoids/chlorophyll A ratio from leaf spectral reflectances. *Photosynthetica* **1995**, *31*, 221–230.
42. Blackburn, G.A. Spectral indices for estimating photosynthetic pigment concentrations: A test using senescent tree leaves. *Int. J. Remote Sens.* **1998**, *19*, 657–675. [[CrossRef](#)]
43. Gitelson, A.A.; Merzlyak, M.N.; Lichtenthaler, H.K. Detection of red edge position and chlorophyll content by reflectance measurements near 700 nm. *J. Plant Physiol.* **1996**, *148*, 501–508. [[CrossRef](#)]
44. Fisher, R.A. *Statistical Methods for Research Workers*; Genesis Publishing Pvt Ltd.: Guildford, UK, 1925.
45. Breiman, L. Random forest. *Mach. Learn.* **2001**, *45*, 5–32. [[CrossRef](#)]
46. Du, P.J.; Samat, A.; Waske, B.; Liu, S.C.; Li, Z.H. Random Forest and Rotation Forest for fully polarized SAR image classification using polarimetric and spatial features. *ISPRS J. Photogramm. Remote Sens.* **2015**, *105*, 38–53. [[CrossRef](#)]
47. Pedregosa, F.; Varoquaux, G.; Gramfort, A.; Michel, V.; Thirion, B.; Grisel, O. Scikit-learn: Machine Learning in Python. *J. Mach. Learn. Res.* **2011**, *12*, 2825–2830.
48. Wu, B.Z.; Liang, A.J.; Zhang, H.F.; Zhu, T.F.; Zou, Z.Y.; Yang, D.M. Application of conventional UAV-based high-throughput object detection to the early diagnosis of pine wilt disease by deep learning. *For. Ecol. Manag.* **2021**, *486*, 118986. [[CrossRef](#)]
49. Tao, H.; Li, C.J.; Zhao, D.; Deng, S.Q.; Hu, H.T.; Xu, X.L.; Jing, W.B. Deep learning-based dead pine tree detection from unmanned aerial vehicle images. *Int. J. Remote Sens.* **2020**, *41*, 8238–8255. [[CrossRef](#)]

**Disclaimer/Publisher’s Note:** The statements, opinions and data contained in all publications are solely those of the individual author(s) and contributor(s) and not of MDPI and/or the editor(s). MDPI and/or the editor(s) disclaim responsibility for any injury to people or property resulting from any ideas, methods, instructions or products referred to in the content.